Local and quantitative measurement of mechanical properties by electrical-nanoindentation in situ SEM: Application to a multi-phase AgCuPd alloy

Chaymaa Boujrouf, Morgan Rusinowicz, Solène Iruela, Annie Antoni-Zdziobek, Yannick Champion, Muriel Braccini, Guillaume Parry, Marc Verdier, Fabien Volpi

Local and quantitative measurement of mechanical properties by electrical - nanoindentation *in situ* SEM: application to a multi-phase AgCuPd alloy

Chaymaa Boujrouf [a,b], Morgan Rusinowicz [a], Solène Iruela [a], Annie Antoni-Zdziobek [a], Yannick Champion [a], Muriel Braccini [a], Guillaume Parry [a], Marc Verdier [a], Fabien Volpi [a]

[a] Université Grenoble Alpes, Grenoble-INP, CNRS, SIMaP, 38000 Grenoble, France

[b] Aix-Marseille University, IM2NP, CNRS, Faculté des Sciences de Saint-Jérôme case 142, 13397 Marseille, France

chaymaa.boujrouf@im2np.fr

Abstract

Nanoindentation has now become the key technique for measuring the mechanical properties of materials at small scales. However, the quantitative and accurate processing of nanoindentation data relies on a physical quantity that is not directly available: the contact area (Ac) between the indenter tip and the sample under test. In complex systems, determining Ac is challenging due to the limitations of standard methods: analytical models have restricted validity domains (sample homogeneity and rheology), and post-mortem observations of residual imprints are time-consuming, do not appraise property gradients and cannot be applied to materials with significant elastic recovery.

In this paper, a comprehensive methodology is proposed to continuously measure contact area during indentation. The proposed methodology, referred to as electrical-nanoindentation (ENI), is based on real-time monitoring of the electrical contact resistance (ECR). The protocol only requires mechanical and electrical calibrations of the indenter tip on reference materials, leading to one-to-one relationship between ECR and contact area. An original approach is also proposed to deal with the presence of surface passivating layers that generally disturb ECR measurements. As an illustration, the methodology is applied to the characterization of a multi-phase alloy (MPA) composed of silver, copper and palladium. This alloy raises the same challenges as those usually faced by nanoindentation in advanced metallurgy: heterogenous distribution of individual phases at the micro-scale, composite response of a complex mixture of hard/stiff and ductile/soft phases,… In addition, the ohmicity of contact is disturbed by surface passivating layers. Despite these numerous hindrances, the proposed methodology is successfully applied to this material. The evolution of contact area is compared with standard methods: an impressive accuracy of less than 2% standard-deviation is achieved when compared to post-mortem observations. The elastic moduli and hardnesses of individual phases are then accurately extracted. In addition, in order to gain in spatial definition, the ENI set-up is integrated into a scanning electron microscope (SEM), enabling indent positioning with a precision close to 100 nm.

Two challenges are successfully met with the ENI methodology. On a mechanical point of view, the response of individual phases can be identified despite the complex rheology of heterogeneous materials, proving the approach applies to all mechanical behaviors (sink-in or pile-up rheologies, homogeneous or heterogeneous materials, with or without elastic recovery,…). On an electrical point of view, even if contact ohmicity is the only requirement of the methodology, it is possible to identify and overcome deviations from contact ohmicity induced by surface passivation. In particular, the non-linear resistive contribution of insulating layers fades during indentation thanks to its dependence as the reciprocal of the square of contact radius. The present work provides the keys to monitoring the contact area on any metallic sample, whether oxide-free or oxidized, making this methodology a promising alternative to standard methods.

Keywords: nanoindentation; ECR; *in situ* SEM; contact area monitoring, mechanical properties of multi-phase alloys

1. Introduction

Nanoindentation is a technique dedicated to the mechanical characterization of materials at the micro/nanometer scale [1], [2], [3][4] . It is widely used for the local measurement of hardness, elastic modulus, as well as for the identification of mechanical constitutive law components (yield strength σ_y, hardening power,…) [1], [2], [5] . Initially applied to characterize the surfaces of bulk and homogeneous materials, nanoindentation has broadened its scope of application to increasingly complex materials: micro/nano-systems, functional thin films [6], [7], multilayer structures [8], [9], [4], multi-phase alloys [10], shape memory alloys [11], pharmaceuticals [12]... In terms of instrumental development, nanoindentation has been the subject of numerous innovations, through its integration into electron microscopes [13], [14], [15], [16], [17] or heating systems [18], [19], [20], [21]. Among other disruptive approaches, nanoindenters have been coupled with electrical measurements, giving rise to electrical-nanoindentation (ENI). ENI extends the sensitivity of nanoindentation to fine physical phenomena such as phase transformations in semiconductors, early damage detection, piezoelectricity/ferroelectricity, incipient plasticity,… [13], [14], [22], [23], [24]. This coupling has also been explored to monitor the contact area between the indenter tip and the sample during indentation. The present article focuses on the latter application.

Standard nanoindentation tests involve the penetration of a rigid hard indenter into the sample to be characterized, applying a mechanical load L which is continuously recorded along with the displacement of the indenter. Hardness H and elastic modulus E are then obtained thanks to the combination of Sneddon relation (equation Equation 2) and equations Equation 1Equation 3:

$$H = \frac{L}{A_c} \qquad \text{Equation 1}$$

$$E^* = \frac{S_c}{2}\sqrt{\frac{\pi}{A_c}} \qquad \text{Equation 2}$$

$$\frac{1}{E^*} = \frac{1-\nu^2}{E} + \frac{1-\nu_{ind}^2}{E_{ind}} \qquad \text{Equation 3}$$

With E^* the so-called reduced elastic modulus, E_{ind} the elastic modulus of the indenter and ν and ν_{ind} the Poisson's ratio of the material and the indentor respectively, S_c the contact stiffness [25] (measured in our set-up by CSM mode: continuous stiffness measurement). A_c is the projected contact area between the tip and the sample.

As these equations show, the extraction of elastic modulus and hardness relies on knowledge of the contact area A_c, which is the main unknown in nanoindentation experiments as there is no direct measure of it during testing [26], [27]. A_c is essentially driven by material rheology [28], [29]: for materials with large σ_y/E_{mat} ratios, the indented surface will tend to sink-in under the tip, whereas materials with low σ_y/E_{mat} ratios will rather pile-up [28]. These different behaviors can introduce errors as large as 60% on the extracted hardness and 30% on the elastic modulus [28]. These points highlight the need for an accurate and robust method to continuously compute the contact area.

An experimental way to access to this contact area is to perform post-mortem imaging of residual imprints (with scanning electron microscopes (SEM) or scanning probe microscopes (SPM)). This method is the most accurate and versatile way as it does not require any model for materials with negligible elastic recovery. However, only one measure of A_c can be performed per indent, meaning that hardness/elastic modulus can only be computed at maximum load and any intermediate data are lost. To circumvent this issue, the mostly used approach is to process nanoindentation data with analytical models. Two models are mainly used by the nanoindentation community, depending on the material rheology. The widely used model proposed by Oliver and Pharr [30] applies to sink-in rheologies, while the model proposed by Loubet et al [3] applies mainly for pile-up rheologies. Like any

analytical approach, these models rely on strong assumptions, i.e. material homogeneity and monotonic rheology. Consequently, they no longer apply to the characterization of heterogeneous systems with complex rheologies (thin films, multi-phased alloys, etc.).

For all these reasons, alternative methods need to be explored. Among them, coupling nanoindentation with electrical measurements appears as a promising way. Early studies on microindentation have shown that electrical measurements can be successfully used to monitor contact area [31]. However, this pioneering work (recently validated on industrial materials showing different rheologies [27]) was performed at a macro-scale, i.e. two orders of magnitude larger than in nanoindentation tests, meaning that small-scale systems (thin films, materials with fine microstructures, surface passivating layer,…) cannot be described. On nanoindentation systems, Ruffel et al. [32] clearly related the continuous current increase during indentation to the evolution of contact area, but this study did not quantitatively track contact area. While indenting metallic glasses, Singh et al. [33] managed to relate discrete ECR drops to contact area increments, further attributed to the nucleation/propagation of shear bands. In this study, contact area was computed after ECR calibration directly on the metallic glass under study. Volpi et al. [34], [35] proposed to monitor contact area by ENI after electrical calibration on a reference material (an oxide-free metal). This approach made it possible to characterize any oxide-free system (or close to be). Although remarkable accuracy was demonstrated on systems with complex rheologies, the "oxide-free" condition remained a major limitation.

In terms of spatial resolution, it should be noted that in most studies, materials were homogeneous, meaning that samples could be tested randomly on their surface. In the case of heterogeneous systems, large matrices of indents need to be run and post-mortem observations combined with statistical analysis are used to discriminate the properties of individual domains. The integration of nanoindenters into imaging devices (SEM or SPM) is mainly used to visualize physical phenomena during indentation [13], [15], [36], [37], but rarely to locate precisely the indents.

In the present work, *in situ* SEM ENI is applied to overcome the two limitations mentioned above: 1/ the presence of a thin passivating layer (oxide or equivalent) on the sample surface which disturbs contact ohmicity and 2/ the heterogeneity of material at a micrometer-scale. For this purpose, a complex system presenting different challenges has been chosen: AgCuPd alloys exhibit micrometer-scale microstructures with the coexistence of several phases presenting different passivated surfaces. AgCuPd alloys are high performance alloys combining high mechanical strength and electrical conduction [38]. They are used in the microelectronics industry to manufacture wires for probe cards, or in the aerospace industry as brazing alloys for electronic devices and aircraft gas turbine engines [39], [40]. Depending on their composition and thermomechanical treatment, several phases (essentially Ag-rich and/or Cu-rich) can coexist at the micrometer scale. Most studies of these alloys focused on their macroscopic properties [38], with only a minority examining the behavior of individual phases [10]. In the present paper, a protocol for the mechanical and electrical calibrations of the ENI system is first described. Then an AgCuPd multi-phase systems is characterized by *in situ* SEM ENI. While the dependence of contact ohmicity is discussed for each phase, data can be converted into contact area which is then compared to post-mortem observations for validation. Thanks to this approach, the local properties of the heterogeneous alloy, hardness and elastic modulus are quantified, overcoming the challenges of small scales, complex mechanical responses, and contact ohmicity.

2. Materials and methods

2.1. Materials

Two AgCuPd specimens were prepared and processed from high purity Ag, Cu, Pd melted by radio frequency induction in an alumina crucible, under He atmosphere. In AgCuPd alloys, three phases with compositional fluctuations can be formed depending on thermomechanical treatments: Ag(Pd) solid solution and two CuPd intermetallic phases, either the disordered A1 phase (face centered cubic) or the ordered B2 phase (simple cubic). Elemental compositions and thermomechanical treatments of the two alloys characterized in the present work are shown in Table 1. The liquid mixtures were maintained at 1570°C during 15 min to ensure good mixing achieved by electromagnetic stirring. For the multi-phase alloy (MPA), strain hardening was obtained by lamination into bars finally drawn to form wires with diameter in the range of 60 µm. For the single-phase alloy (SPA), no strain hardening was carried out. Finally, both samples were annealed at 550°C for one month. After preparation, samples were mounted for grinding and polishing. Cross-sections were obtained by fine polishing: first, samples were mechanically polished with the SiC papers with grit sizes down to 5 µm, followed by multistep mirror polishing with 3 µm and 1 µm diamond suspension. Then, samples were polished by VibroMet (Vibratory Polisher) with suspension mixture of 0.06 µm of colloidal silicon and 0.05 µm of alumina.

Specimen	Name	Ag (at%)	Cu (at%)	Pd (at%)	Strain hardening (rat%)	Annealing temperature (°C)	Annealing duration (month)
Multi-Phase Alloy	MPA	37.5 (+/- 2.5)	37.5 (+/- 2.5)	27.5 (+/- 2.5)	88	550	1
Single-Phase Alloy	SPA	3 (+/- 0.5)	57 (+/- 0.5)	40 (+/- 0.5)	None	550	1

Table 1 : Elemental compositions and thermomechanical treatments of the two alloys characterized in the present work.

2.2. Electrical-nanoindentation set-up and *in situ* SEM-integration

The ENI instrument (Fig. 1) was essentially home-developed at SIMaP lab. It combines a force-controlled actuator (“1” in Fig. 1) from KLA-Tencor equipped with the Continuous Stiffness Measurement (CSM) mode [30], piezoelectric translators from SmarAct, and a fully-guarded measurement chain for electrical measurements. A cube-corner geometry was chosen for the indenter tip, in order to reduce the size of indented volume. The sample (“7” in Fig. 1) was polarized either at 2 V for continuous measures or from 0.25 to 2 V for current-voltage (I-V) characteristics. The electric current flowing through the tip was measured through a dedicated set-up (“3” to “5” in Fig. 1) with a ResiScope module from Scientec [41]. The electrical contact resistance was then simply computed as the ratio between polarization bias (V) and measured current (I): $R = V/I$. The whole set-up was then integrated into a scanning electron microscope with field emission gun (SEM-FEG), a GEMINI SEM 500 from Zeiss. The set-up optimization allows the indent positioning with a precision better than 100 nm. More details are available here [35], [36]. A gold single-crystal was also used for the electrical calibration step, as described in [35].

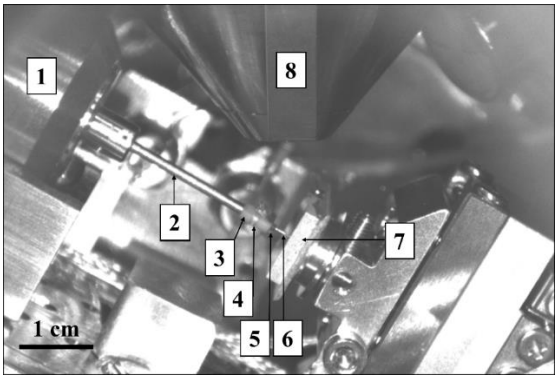

Fig. 1. Infrared view of the ENI device once integrated into the SEM (1 = Nanoindenter head, 2 = Metallic extender, 3 = Ceramic element, 4 = Guard ring, 5 = Brass eyelet, 6 = Tip, 7 = Sample, 8 = SEM column).

2.3. Microstructural characterizations

The sample microstructures were characterized by SEM, on an Ultra 55 from Zeiss equipped with Field Emission Gun (FEG) source. Optimum BSD contrast was obtained for an acceleration voltage of 10 keV and a working distance of 13 mm.

Metallurgical phases were identified by X-Ray Diffraction (XRD). XRD analyses were carried out with a PANalytical X'Pert PRO Multi Purpose Diffractometer. X-Ray source was a copper anode with wavelength $K_\alpha = 1.5419$ Å. Acquisitions were performed in Bragg-Brentano configuration in a $\theta/2\theta$ geometry. Sample was fixed on the stage, rotating at an angular speed θ of 15 rpm, and the detector scan speed 2θ was between 0.6 and 1.26 °/min.

Elemental composition was determined by Electron Probe Micro-Analysis (EPMA), on a CAMECA SX50 electron microprobe automated by SAMx software. It is equipped with 4 wavelength-dispersive spectrometers (WDS) with conventional or multi-layer crystals. Analysis was performed in point probe mode with an acceleration voltage of 20 kV and a probe current 60 nA.

3. Results

3.1. Microstructure characterization and phase identification

Fig. 2-a and Fig. 2-b present SEM micrographs of samples MPA and SPA, respectively. While SPA sample appears as highly homogeneous, MPA sample presents heterogeneous microstructure at the micrometer scale. Three different domains can be observed on the MPA sample (circled on Fig. 2-a). The chemistry of these domains was identified by EPMA analysis (not shown): the brightest domains are Ag-rich, while the uniform grey domains and the heterogeneous dark/white domains are essentially Cu-rich. Dealing with the SPA sample, the homogeneous phase carries the chemical composition of the initial alloy (see Table 1), it is essentially a solid solution of Cu-rich phase.

Fig. 2-c and Fig. 2-d present XRD diffractograms of samples MPA and SPA, respectively. On the MPA sample, three phases are detected. First, a face centered cubic (fcc) Ag-rich solid-solution is identified and can be attributed to the brightest domains observed by SEM. This phase will be referred to as the "Ag-rich phase". Then, two CuPd phases with distinct crystalline structures are identified. The prevailing phase is the ordered B2 simple cubic (sc) phase, which in turn can be attributed to the uniform grey domains observed by SEM. This phase will be referred to as the "Cu-rich phase". Finally, a weaker contribution of the disordered A1 fcc CuPd phase is observed. This fcc CuPd phase, which is richer in Cu than the sc CuPd, phase, gives the darkest signature within the heterogeneous dark/white domains observed by SEM (further referred to as "mixture domain"). On the SPA sample, only the ordered B2 simple cubic CuPd phase is observed (a negligible signature of the A1 CuPd phase is weakly observed). This single-phase identification is in accordance with SEM observations.

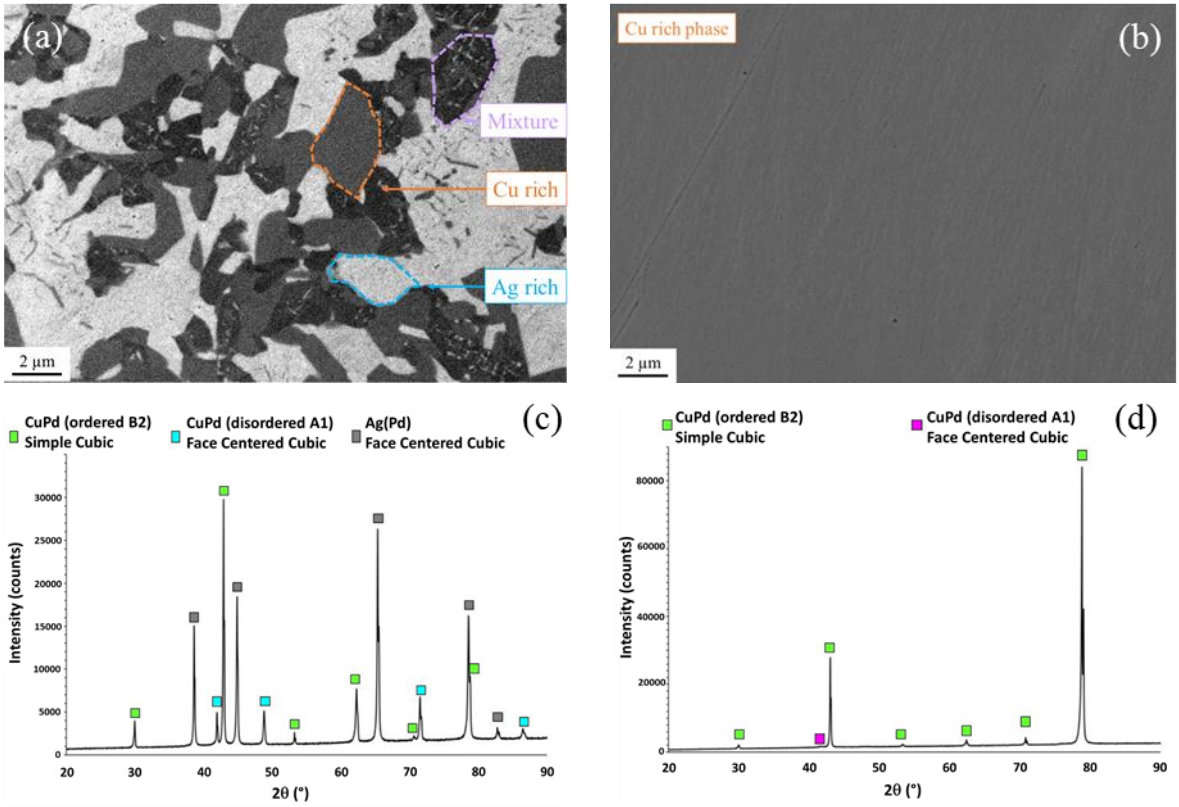

Fig. 2. (a, b) SEM-BSD micrographs depicting the MPA and SPA samples, respectively, and (c, d) the corresponding XRD diffractograms.

3.2. Indenter tip mechanical and electrical calibrations

The quantitative monitoring of contact area by ENI relies on the initial mechanical and electrical calibrations of the indenter tip [35]. The mechanical calibration step relates contact depth (h_c) to contact area/radius (A_c or r_c, respectively), thus leading to the so-called area function [26]. On the other side, the electrical calibration step relates electrical contact resistance (R) to contact depth (h_c). The reference method for mechanical calibration is the Oliver-Pharr method applied to fused silica [30]. However, in the present case, the use of a cube-corner geometry leads to early cracking [42]. Cracking occurs for penetration depths of 400-500 nm (i.e. for contact depths ~300 nm) which prevents tip calibration beyond these shallow penetrations. Thus, another method was employed to determine the tip area function. Bulk gold single-crystal was indented at 10 different depths ranging from 100 nm to 1000 nm (9 tests for each depth), and the areas of residual imprints were measured by post-mortem SEM observations. The Oliver-Pharr model was then applied to convert penetration depth into contact depth, thanks to the absence of pile-up, even at large depths. Finally, the SEM-measured contact areas A_c were plotted against Oliver-Pharr contact depths h_c before fitting by polynomial regression, thus giving the tip area function. The overall machine stiffness has been measured independently to 9.10^5 N/m. Fig. 3Fig. 3- a reports the area function of the present cube-corner indenter obtained by this method. Up to $h_c \sim 300\ nm$, the curve overlaps with the calibration on fused silica. For larger depths, the "fused silica" extrapolation becomes invalid because of silica cracking.

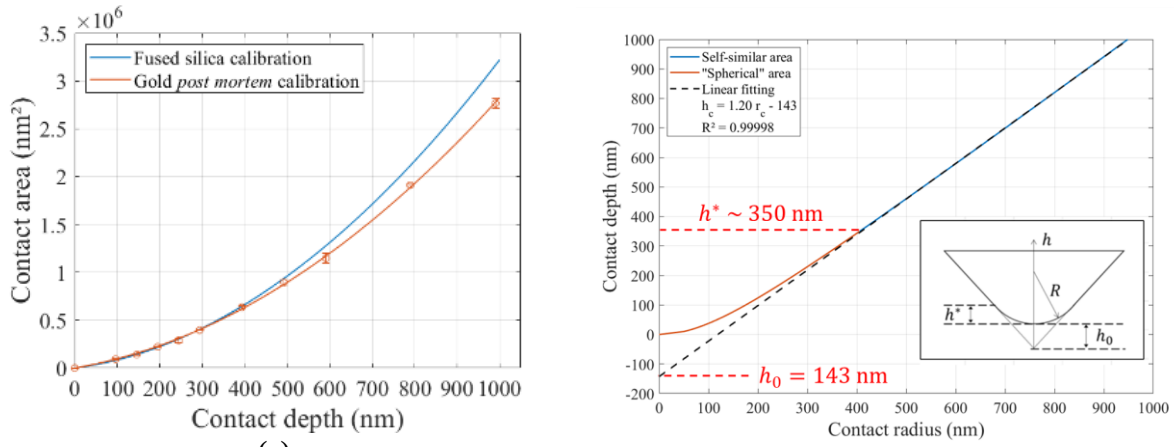

Fig. 3. (a) Area function of the cube-corner tip. The extrapolated calibration obtained with fused silica is shown to illustrate deviation beyond 300nm, thus justifying the calibration performed on gold sample. (b) Tip profile with blunt and self-similar domains. Defect features are illustrated in inset figure, with R is the tip radius of curvature.

From this mechanical calibration, the characteristic features of the so-called "tip defects" can be identified (inset in Fig. 3-b). The first defect feature is the height h^* of the blunt apex. It represents the height beyond which the indenter becomes self-similar. To estimate h^*, the derivative of contact radius with respect to contact height is plotted against contact height using the previously determined area function. The depth at which the derivative $\mathrm{d}r_c/\mathrm{d}h_c$ becomes constant is h^*. The second defect feature, h_0, representing the missing apex of the indenter tip, was estimated by plotting contact height against contact radius using the determined area function. The y-intercept obtained from the linear extrapolation of the self-similar domain ($h_c > h^*$) is h_0. Fig. 3-b reports these tip defect features $h^*$and h_0, measured to 350 nm and 143 nm, respectively. The linear relationship between contact depth and contact radius is clearly observed beyond contact depth of 350 nm (self-similar domain), with a slope of 1.2.

For the electrical calibration step, electrical contact resistance was continuously measured during indentations on the bulk gold single-crystal. Indents at different bias voltages (0.5 V, 1.25 V, 2 V, and

4 V) were performed (9 tests for each voltage). Reproducible resistance-depth curves indicate a perfectly ohmic contact, independent of the voltage. This electrical calibration step followed the method described in details in [35]. For each test the electrical resistance was plotted against the reciprocal of the corrected contact depth, $R = f(1/h_c + h_0)$ (Fig. 4-a). Contact depth was determined using the already validated Oliver-Pharr model for gold, while the tip defect h_0 was known from mechanical calibration. As electrical contact is ohmic, the electrical resistance should vary linearly with the reciprocal of the corrected contact depth in the self-similar domain of the indenter (i.e. for $h_c > h^*$). This is confirmed on the zoom-in shown in Fig. 4-b.

Note that the spreading resistance within the sample (R_{Sample}) is caused by the constriction of current lines to the contact and is proportional to the sample's resistivity. Since the resistivity of standard metals is 5 orders of magnitude lower than that of the BDD-tip, this spreading resistance can be safely ignored for upcoming analysis [35]. As already reported [34], [35], this electrical calibration on a reference material (i.e. free from any insulating surface layer like oxide, sulfide, organic contaminant,...) can be modelled by a simple expression (Equation 4) :

$$R = R_0 + \frac{\rho_0}{h_c + h_0} \qquad \text{Equation 4}$$

With R_0 and ρ_0 two calibration coefficients independent of the reference sample if its resistivity is much lower than that of the tip. R_0 represents the setup series resistance, and ρ_0 is driven by the tip resistivity and geometry. In the present case, linear regression yields to $R_0 = 438\ \Omega$ and $\rho_0 = 2.39\ 10^6\ \Omega.\text{nm}$, for a validity domain beyond $h_c > 350\ nm$.

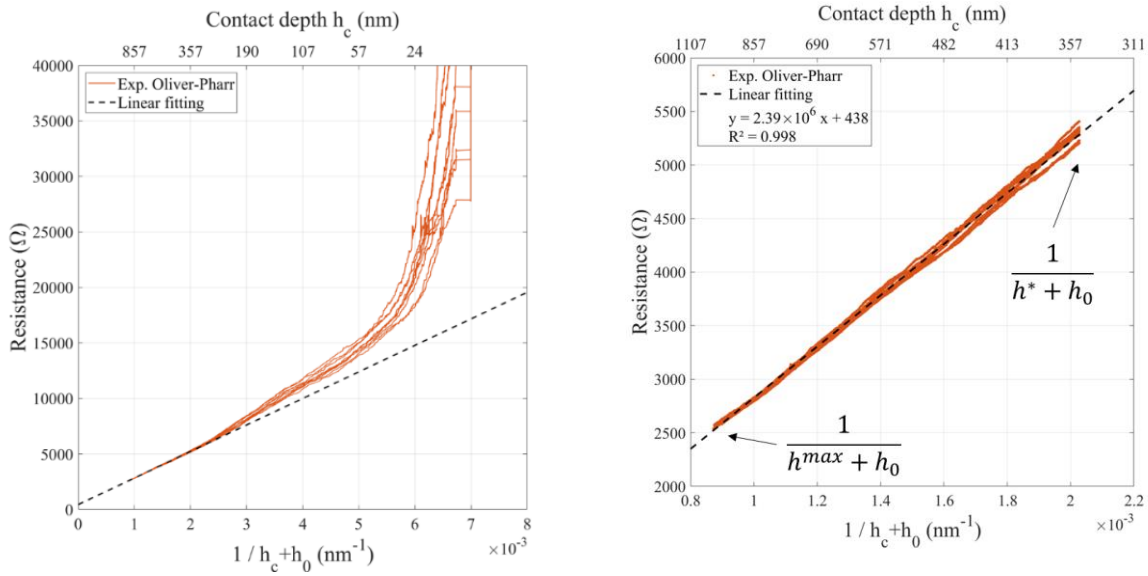

Fig. 4. (a) Evolution of electrical resistance with the reciprocal of the corrected contact depth. (b) Zoom-in on self-similar range (from h^* to h_{max}). Linear regression coefficients R_0 and ρ_0 for electrical calibration are given in the inset.

3.3. Local measures on the individual phases of the multi-phase alloy (MPA)

Once the indenter tip fully calibrated, the monitoring of contact area can be conducted on the sample of interest (the multi-phase AgCuPd alloy in the present case). Thanks to SEM coupling, Ag-rich and Cu-rich phases were targeted by positioning the indenter at the center of the respective domains (Fig. 5). Precision of ~ 100 nm was obtained. This precise positioning ensures great sensitivity to the behavior of individual phases. The alternative would be to perform large blind matrices of indents, followed by

tedious statistical processing of imprints, depending on their positioning on the various phases. This possibility was assessed but it demonstrated a success rate as low as ~5% (rate of indents falling at the center of a domain). Series of indents were then performed in each phase at various penetration depths (300, 500 and 1000 nm). The tests were conducted at a bias voltage of 2 V.

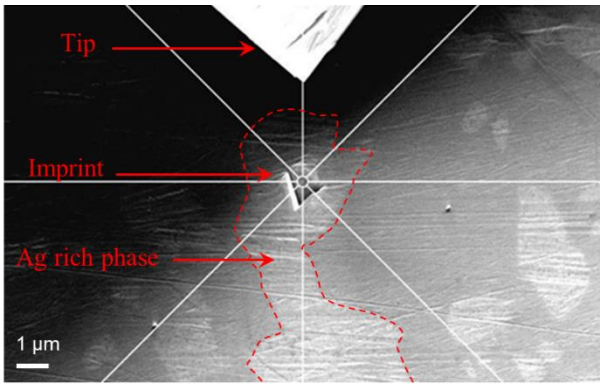

Fig. 5. SEM micrograph showing tip and imprint left after indentation on the Ag-rich phase during an *in situ* SEM experiment.

Fig. 6-a and Fig. 6 -b show representative load-penetration depth ($L-h$) and stiffness-penetration depth ($S-h$) curves for the Cu-rich (red shades) and Ag-rich (blue shades) phases at different depths. The curves exhibit high reproducibility for each phase. In terms of relative trends, the Cu-rich phase require higher loads than the Ag-rich phase (~5 mN and ~2 mN to achieve a depth of 500 nm, respectively). Furthermore, the Cu-rich phase exhibits higher contact stiffness than the Ag-rich phase for a fixed depth, indicating its greater stiffness and/or hardness.

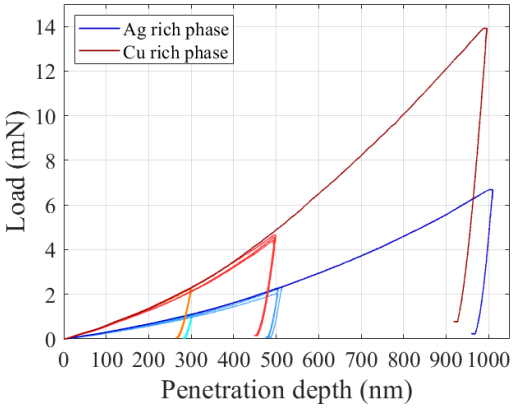

(a)

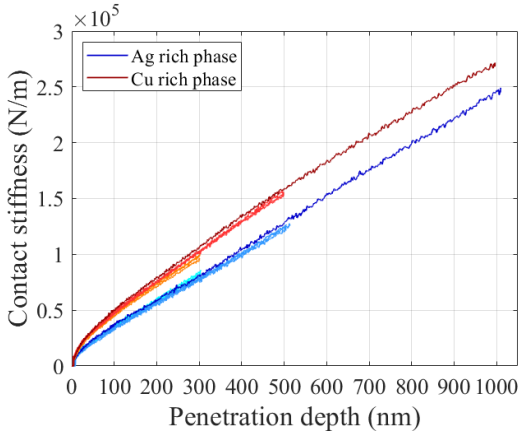

(b)

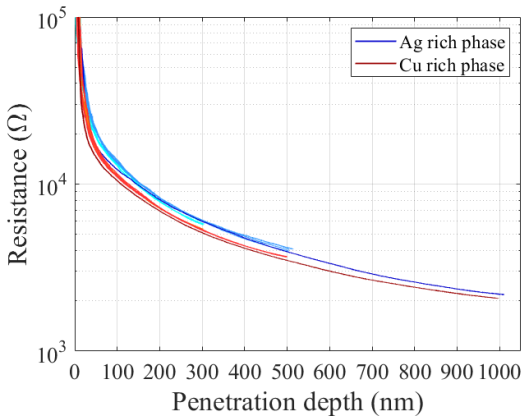

(c)

Fig. 6. (a) Load, (b) stiffness and (c) electrical contact resistance at 2 V curves obtained on MPA sample for three illustrative tests at 300 and 500 nm, and one test at 1000 nm for each individual phase.

The continuous measurement of electrical resistance is also reported (Fig. 6-c). Two distinct behaviors are observed on the two phases, and are highly reproducible. For a given penetration depth, the electrical resistance is consistently lower on the Cu-rich phase compared to the Ag-rich phase. Interestingly, this lower electrical resistance suggests a larger contact area for the Cu-rich phase than for the Ag-rich phase at a given depth. This contradicts the mechanical curves, where the Cu-rich phase is expected to be harder than the Ag-rich phase, implying a smaller contact area for Cu-rich. This higher resistance of the Ag-rich phase can be explained by the presence of an insulating layer on its surface. In order to investigate this electrical behavior, current-voltage (I-V) characteristics were examined. A new series of indentation tests were then conducted and stopped at various penetration depths (50, 100, 200, 300 and 500 nm). At each intermediate depth, a voltage sweep from 0.25 to 2 V with a step of 0.25 V was performed.

The I-V characteristics obtained on the Ag-rich and Cu-rich phases are shown in Fig. 7-a and Fig. 7-b, respectively. These curves result from averaging 8 tests at each penetration depth. On both phases, good linearity is observed at large depth, suggesting an ideal ohmic behavior. However, deviation from linearity seems to affect the shallow-depth tests. In order to analyze quantitatively this trend, focus is made on the quasistatic resistances (V/I ratios) that should be constant with voltage if contact is ohmic. For comparison's sake, quasistatic resistances are normalized to a reference resistance (the resistance obtained at 2 V for each depth). The dependence of this normalized resistance with the applied voltage is shown in Fig. 7-c and Fig. 7-d for the Ag-rich and Cu-rich phases, respectively. On both phases, deviation from ideality is observed at shallow depths (up to 30% deviation). The ohmicity domain can be defined arbitrarily to deviations lower than 3% (corresponding to a threshold of 103% for the normalized resistance). This arbitrary "3%" threshold is a highly stringent criterion that could be extended, what would reduce the cut-off penetration depth. With this stringent criterion, contact ohmicity on the Ag-rich phase is ensured beyond penetration depth of 200 nm (Fig. 7-c). For the Cu-rich phase, the "3%" threshold is reached as early as 100 nm (Fig. 7-d). The non-linearity observed at shallow depths can be attributed to surface modifications during sample preparation: while a Cu oxide is expected to grow on the Cu-rich phase surface, a Ag sulfide has been detected by XPS (not shown) on the Ag-rich phase after some sample preparations, in accordance with [43]. These surface layers contribute to the overall measured resistance by adding an extra voltage-dependent resistance that evolves as the reciprocal of r_c^2 [35], [43]. This latter point explains why this non-ohmic resistance fades with deeper indentation, since the other contributions evolve as the reciprocal of r_c (Equation 4). In Fig. 7 (c), the error bar size for the 50 nm measurement is larger than the corresponding depth condition

for the Cu-rich phase in Fig. 7 (d). This discrepancy can be attributed to the variability in the behavior and resistivity of silver sulfides compared to copper oxide.

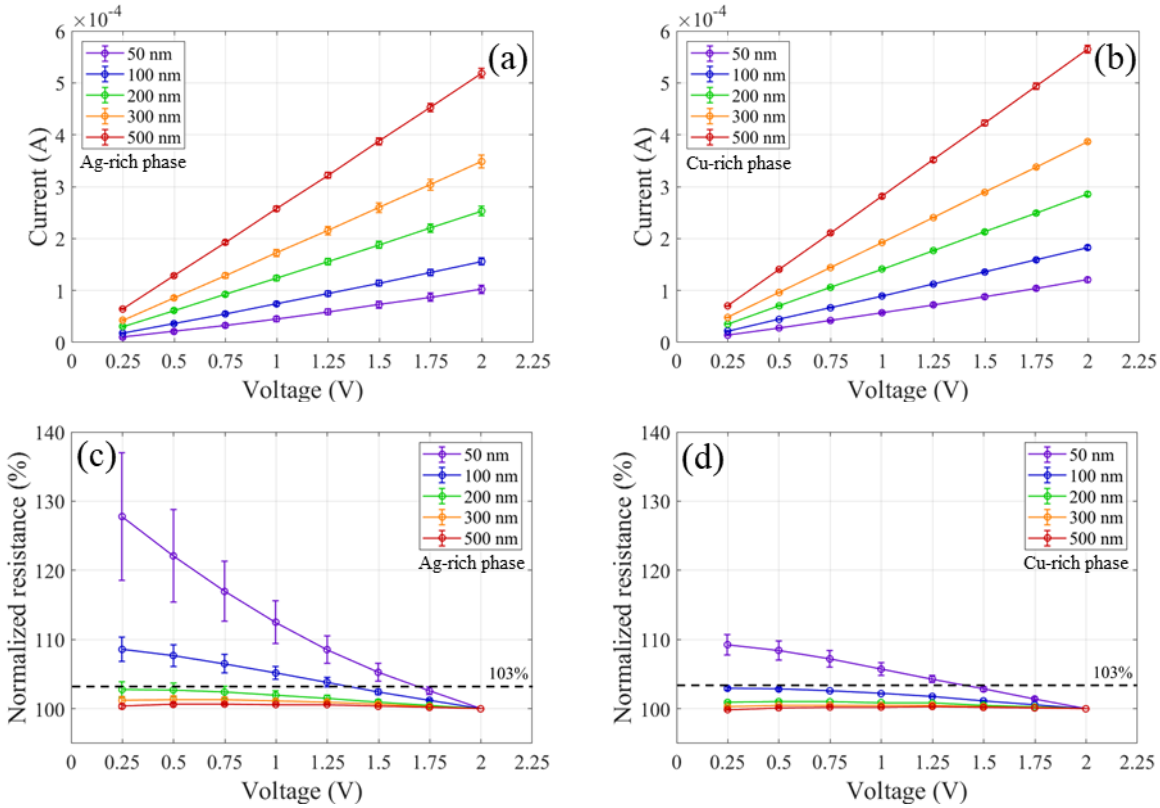

Fig. 7 (a, b) Current-voltage characteristics on the Ag-rich and Cu-rich phases, respectively, and (c, d) Normalized resistance as a function of applied voltage at different depths for the (a, c) Ag-rich phase and (b, d) Cu-rich phase.

Whatever the origin of these non-linearities, all data beyond penetration depths of 200 nm are ohmic on both phases, meaning that they can be processed to monitor the evolution of contact area. Thanks to the electrical calibration, the resistance data were converted into contact depth data, that were then converted into contact areas thanks to the mechanical calibration. In order to validate these results, post-mortem SEM measurements were conducted to determine the areas of residual imprints. Results, as well as comparisons with Oliver-Pharr and Loubet models, are shown in Fig. 8-a and Fig. 8-b, respectively. Numerical data and deviations to post-mortem observations are given in Table 2.

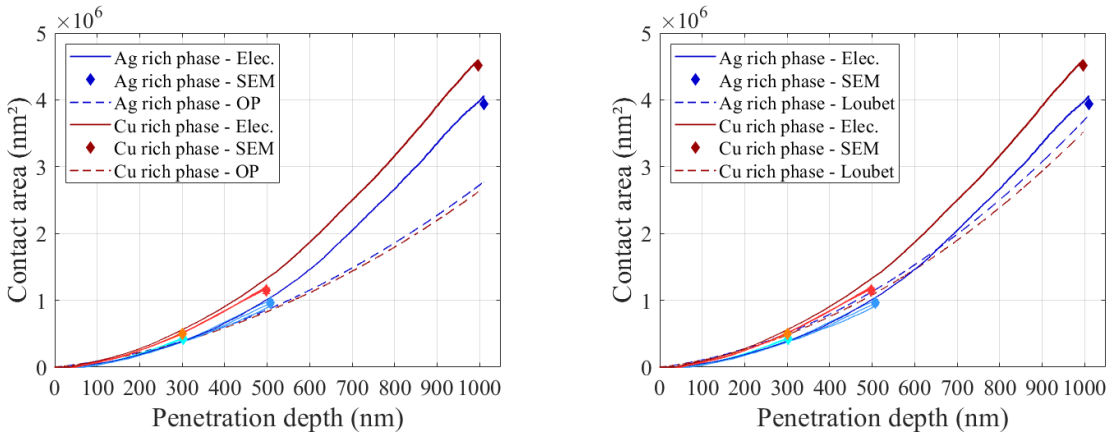

(a) (b)

Fig. 8. Comparison between electrical monitoring of contact areas on both phases and post-mortem measured contact areas, compared to (a) Oliver-Pharr and (b) Loubet models.

As can be seen, an excellent agreement is observed on both phases between the contact areas predicted by the present approach and post-mortem measurements. An average standard deviation of 1.75% is obtained between the ENI predictions and post-mortem observations, thus fully validating the developed methodology. Dealing with the model predictions, it can be seen that the Oliver-Pharr model always underestimates the areas (due to its "sink-in" assumption that does not apply on these ductile materials), with an average standard deviation of 22.5%. Even if it is much closer thanks to its "pile-up" assumption, the Loubet model also fails to describe the complex rheology of this heterogeneous multi-phase system, with an average standard deviation of 13.0%. Furthermore, the two models reverse the trends of the two phases.

Phase	Penetration depth (nm)	Ac - PM (nm^2)	Ac - ENI (nm^2)	Ac - OP (nm^2)	Ac - L (nm^2)	SD - ENI/PM	SD - OP/PM	SD - L/PM
Ag-rich	300	4.18×10^5	4.19×10^5	3.99×10^5	5.13×10^5	0.01%	-4.54%	22.68%
Cu-rich	300	4.94×10^5	4.98×10^5	3.80×10^5	4.81×10^5	0.86%	-23.00%	-2.56%
Ag-rich	500	9.60×10^5	9.53×10^5	8.79×10^5	1.16×10^6	-0.72%	-8.43%	20.78%
Cu-rich	500	1.14×10^6	1.19×10^6	8.28×10^5	1.08×10^6	4.01%	-27.57%	-5.65%
Ag-rich	1000	3.94×10^6	4.06×10^6	2.77×10^6	3.77×10^6	2.95%	-29.58%	-4.32%
Cu-rich	1000	4.51×10^6	4.60×10^6	2.62×10^6	3.52×10^6	1.94%	-41.91%	-22.09%
Average						1.75%	22.5%	13.0%

Table 2. Contact areas determined by post-mortem SEM measurements (PM), electrical-nanoindentation (ENI), Oliver-Pharr (OP) and Loubet (L) models. Standard deviations (SD) to post-mortem observations are also given.

3.4. Application and discussion

As the monitoring of contact area is validated, the micrometric mechanical properties of both phases can be determined continuously during indentation thanks to equationsEquation 1 and Equation 2. Fig.Fig. 9-a andFig. 9-b report the elastic modulus and hardness curves of AgCuPd phases as a function of penetration depth. As mentioned earlier, two validity domains have to be considered. The linear relationship of the mechanical calibration applies for contact depth beyond 350 nm, while ohmicity is only ensured beyond penetration depth of 200 nm. Regarding the first cut-off depth, its conversion into contact area (thanks to Fig. 3) leads to an area of $\sim 0.5 \times 10^6\ nm^2$. According to Fig. 8Fig. 8, this area corresponds to a penetration depth of ~300 nm. Consequently, this first cut-off depth prevails over the

"ohmicity" limitation (200 nm), and the three tested depths (300, 500 and 1000 nm) belong to the validity domain of our method. All mechanical data beyond penetration depth of 300 nm are then acceptable. Also noteworthy is that the most limiting criterion in the present method is the linearity of mechanical calibration (Fig. 3). Even though analytical processing remains the most easy-to-use method, the numerical fitting of area function could further extend the validity domain down to the "ohmicity" criterion.

In order to further complete the validation of our approach, the mechanical properties of the Cu-rich phase were measured independently on SPA sample, which is a single-phase CuPd reference sample (Fig. 2(b, d)). SPA sample was indented at various depths, and post-mortem SEM observations of residual imprints were performed, thus excluding the use of models for this sample. Results are reported in Fig. 9. Once more, excellent agreement is observed with the "electrical" data beyond 300 nm, for both elastic modulus and hardness.

In terms of mechanical properties, the elastic modulus of the Cu-rich and Ag-rich phases are rather steady between 300 and 500 nm, and measured at 121 ± 2 GPa and 108 ± 3 GPa at 500 nm depth, respectively. Beyond 500 nm, the composite response of this multi-phase system is observed, with a merging of the elastic responses [44]. Regarding hardness, values of 3.80 ± 0.13 GPa for the Cu-rich phase and 2.30 ± 0.21 GPa for the Ag-rich phase at 500 nm depth are obtained. The continuous decrease of hardness can be either attributed to surface hardening during sample polishing or to indentation size effect [5], [45]. These raw indentation data could now be used as inputs for numerical modelling to more accurately discriminate the contributions of each phase [44].

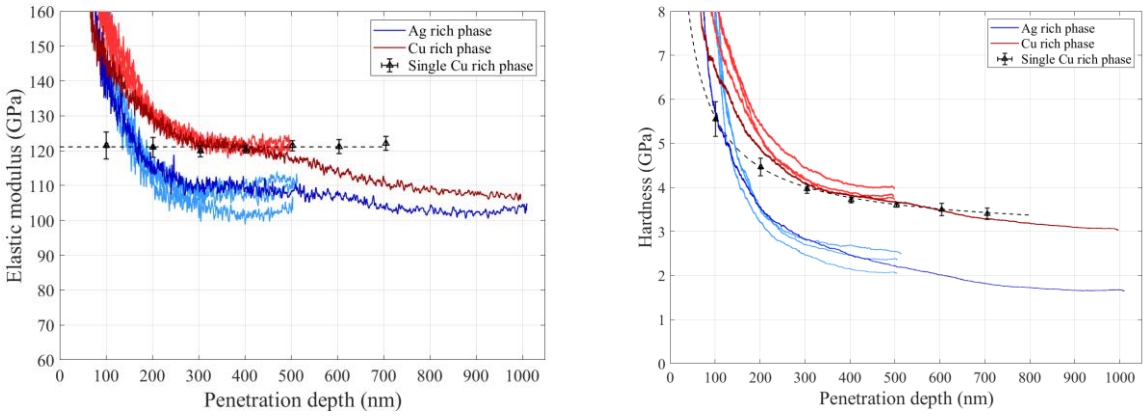

(a) (b)

Fig. 9. Evolution of elastic modulus (a) and hardness (b) determined by electrical monitoring on MPA sample as a function of penetration depth. Data obtained on SPA sample are also reported for comparison with the copper-rich phase. The light red (blue as well) colors corresponds to the 500 nm penetration depth. The darker colors correspond to the 1000 nm penetration depth.

Finally, deviations from ideality of the electric contact (Fig. 7) open to an estimation of the effective contact resistivity ρ_c of the passivating films. Indeed, the difference to the ideal resistance, which includes only the tip and setup resistances (Equation 5), is the extra-contribution due to the non-linear passivating layer sandwiched at the tip-to-sample interface. According to [43], this latter contribution can be expressed as:

$$R_{Interface} = \frac{\rho_c}{A_c} \qquad \text{Equation 5}$$

ρ_c can then be estimated in the worst case on the Ag-rich phase, i.e. for bias voltage = 0.25 V and penetration depth = 50 nm, as can be seen in Fig. 7. A value of $3.10^{-6}\ \Omega.cm^2$ ($\pm 50\%$) is obtained. Such a low contact resistivity might be explained by the local high mechanical pressure.

4. Conclusions

In this work, the coupling of nanoindentation with *in situ* SEM electrical measurements was used to continuously monitor the contact area during indentation of a system with complex rheology. Contact area is the cornerstone of quantitative processing of nanoindentation data. Its monitoring has been applied to the quantitative extraction of hardness and elastic modulus of Cu-rich and Ag-rich phases of an AgCuPd alloy. The challenge for the characterization of this system was twofold: from a mechanical point of view, its individual phases presented rather different pile-up rheologies, and from an electrical point of view, the surfaces of the two phases were covered by an insulating layer that disturbed the contact ohmicity.

The first step of the protocol involves mechanical and electrical calibrations of the indenter tip. In the present case, the area function of the cube-corner tip is essentially obtained by post-mortem observations of indents on a gold single crystal, in order to overcome the limitation imposed by silica cracking. Electrical calibration is carried out by electrically-indenting a gold single crystal, in order to establish a "resistance vs contact depth" relationship.

The electrical-nanoindentation testing of the AgCuPd system was then performed *in situ* SEM. SEM imaging was used to precisely target the micro-scale phases to be analyzed, with a precision close to 100nm. Because of the top-surface insulating layers on both Cu- and Ag-rich phases, contact ohmicity was compromised on both phases for shallow indents but was restored beyond threshold contact depths (100 nm and 200 nm, respectively). Thanks to the calibration steps, electrical-nanoindentation data were then processed to extract the contact area evolution during indentation. Post-mortem observations of the imprints were then compared with our predictions. Excellent agreement was then observed, whereas standard analytical models proved unable to predict the contact areas on both phases. These results fully validate the proposed approach for contact area monitoring, thus opening to the extraction of hardness and elastic modulus of both Cu- and Ag-rich phases. The values obtained on the Cu-rich phase were then compared to data obtained independently on a reference single phase sample, confirming the validity of the approach.

The present work provides the keys to monitoring the contact area on any metallic sample, from oxide-free to oxidized metals. It therefore appears to be a promising alternative to the analytical models used as standard. Challenging prospects are the tailoring of the present approach to dielectric/insulating substrates.

Aknowledgements

This work was supported by the Centre of Excellence of Multifunctional Architectured Materials "CEMAM" which is a program funded by the French National Research Agency (ANR) [grant numbers ANR-10-LABX-44-01] and by the Institut Carnot "Energies du Futur".

The authors would like to thank the staff from the CMTC platform (https://www.cmtc.grenoble-inp.fr): F. Charlot, R. Martin and F. Roussel-Dherbey for the support with in situ SEM experiments, F. Robaut for EPMA measurements and S. Coindeau and T. Encinas for XRD measurements.

Data availability

The raw/processed data required to reproduce these findings cannot be shared at this time due to technical or time limitations.

V. References

[1] M. F. Doerner and W. D. Nix, "A method for interpreting the data from depth-sensing indentation instruments," *Materials Research Society*, vol. 1, no. 4, pp. 601–609, 1986, doi: https://doi.org/10.1557/JMR.1986.0601.

[2] J. B. Pethica, R. Hutchings, and W. C. Oliver, "Hardness measurement at penetration depths as small as 20 nm," *Philosophical Magazine A*, no. 48:4, pp. 593–606, 1983.

[3] LL. Loubet, M. Bauer, A. Tonck, S. Bec, and B. Gauthier-Manuel, "Nanoindentation with a surface force apparatus," *Mechanical Properties and Deformation Behavior of Materials Having Ultra-Fine Microstructures*, vol. 429–447, 1993.

[4] Y. I. Golovin, "Nanoindentation and mechanical properties of solids in submicrovolumes, thin near-surface layers, and films: A Review," *Physics of the Solid State*, vol. 50, no. 12, pp. 2205–2236, Dec. 2008, doi: 10.1134/S1063783408120019.

[5] A. C. Fischer-Cripps, *The IBIS Handbook of Nanoindentation*. Fischer-Cripps Laboratories Pty Ltd, 1968. Accessed: Dec. 14, 2021. [Online]. Available: www.fclabs.com.au

[6] R. Saha and W. D. Nix, "Effects of the substrate on the determination of thin film mechanical properties by nanoindentation," *Acta Mater*, vol. 50, no. 1, pp. 23–38, 2002, doi: https://doi.org/10.1016/S1359-6454(01)00328-7.

[7] T. Y. Tsui and G. M. Pharr, "Substrate effects on nanoindentation mechanical property measurement of soft films on hard substrates," *J Mater Res*, vol. 14, no. 1, pp. 292–301, 1999, doi: 10.1557/JMR.1999.0042.

[8] J. Chen and S. J. Bull, "Assessment of the toughness of thin coatings using nanoindentation under displacement control," *Thin Solid Films*, vol. 494, no. 1–2, pp. 1–7, 2006, doi: 10.1016/j.tsf.2005.08.176.

[9] Q. Wang, F. Zhou, and J. Yan, "Evaluating mechanical properties and crack resistance of CrN, CrTiN, CrAlN and CrTiAlN coatings by nanoindentation and scratch tests," *Surf Coat Technol*, vol. 285, pp. 203–213, 2016, doi: 10.1016/j.surfcoat.2015.11.040.

[10] C. Iwamoto, F. Watanabe, and R. Koitabashi, "Microstructure and mechanical properties of a cu-pd-ag alloy wire with aging treatment," *Materials Science Forum*, vol. 941, pp. 1167–1172, 2018, doi: 10.4028/www.scientific.net/MSF.941.1167.

[11] V. V. Shastry and U. Ramamurty, "Simultaneous measurement of mechanical and electrical contact resistances during nanoindentation of NiTi shape memory alloys," *Acta Mater*, vol. 61, no. 14, pp. 5119–5129, 2013, doi: 10.1016/j.actamat.2013.04.049.

[12] S. Varughese, M. S. R. N. Kiran, U. Ramamurty, and G. R. Desiraju, "Nanoindentation in crystal engineering: Quantifying mechanical properties of molecular crystals," *Angewandte Chemie - International Edition*, vol. 52, no. 10. Wiley-VCH Verlag, pp. 2701–2712, Mar. 04, 2013. doi: 10.1002/anie.201205002.

[13] H. Nili, K. Kalantar-Zadeh, M. Bhaskaran, and S. Sriram, "In situ nanoindentation: Probing nanoscale multifunctionality," *Prog Mater Sci*, vol. 58, no. 1, pp. 1–29, 2013, doi: 10.1016/j.pmatsci.2012.08.001.

[14] J. George, S. Mannepalli, and K. S. R. N. Mangalampalli, "Understanding Nanoscale Plasticity by Quantitative In Situ Conductive Nanoindentation," *Adv Eng Mater*, vol. 23, no. 9, pp. 1–72, 2021, doi: 10.1002/adem.202001494.

[15] R. Rabe *et al.*, “Observation of fracture and plastic deformation during indentation and scratching inside the scanning electron microscope,” *Thin Solid Films*, vol. 469–470, pp. 206–213, 2004, doi: 10.1016/j.tsf.2004.08.096.

[16] S. Kondo, N. Shibata, T. Mitsuma, E. Tochigi, and Y. Ikuhara, “Dynamic observations of dislocation behavior in SrTiO 3 by in situ nanoindentation in a transmission electron microscope,” *Appl Phys Lett*, vol. 100, no. 18, p. 181906, 2012, doi: 10.1063/1.4710558.

[17] X. Li and A. M. Minor, “In situ TEM Investigation of the Electroplasticity Phenomenon in Metals,” *Microsc. Microanal*, vol. 25, no. Suppl 2, pp. 1832–1833, 2019, doi: https://doi.org/10.1017/S1431927619009899.

[18] M. Conte, G. Mohanty, J. J. Schwiedrzik, J. M. Wheeler, J. Michler, and N. X. Randall, “Novel high temperature vacuum nanoindentation system with active surface referencing and non-contact heating for measurements up to 800 ° C Novel high temperature vacuum nanoindentation system with active surface referencing and non-contact heating for me,” *Review of Scientific Instruments*, vol. 90, no. 4, p. 045105, 2019, doi: 10.1063/1.5029873.

[19] G. Tiphéne *et al.*, “High - Temperature Scanning Indentation : A new method to investigate in situ metallurgical evolution along temperature ramps,” *J Mater Res*, vol. 36, no. 12, pp. 2383–2396, 2021, doi: 10.1557/s43578-021-00107-7.

[20] C. Minnert, W. C. Oliver, and K. Durst, “New ultra-high temperature nanoindentation system for operating at up to 1100 °C,” *Mater Des*, vol. 192, Jul. 2020, doi: 10.1016/J.MATDES.2020.108727.

[21] J. S. K. L. Gibson, S. Schröders, C. Zehnder, and S. Korte-Kerzel, “On extracting mechanical properties from nanoindentation at temperatures up to 1000°C,” *Extreme Mech Lett*, vol. 17, pp. 43–49, Nov. 2017, doi: 10.1016/J.EML.2017.09.007.

[22] J. E. Bradby and J. S. Williams, “In situ electrical characterization of phase transformations in Si during indentation,” pp. 1–9, 2003, doi: 10.1103/PhysRevB.67.085205.

[23] M. Huang, T. A. Pascal, H. Kim, W. A. Goddard, and J. R. Greer, “Electronic-Mechanical Coupling in Graphene from in situ Nanoindentation Experiments and Multiscale Atomistic Simulations,” *Nano Lett*, vol. 11, no. 3, pp. 1241–1246, 2011, doi: https://doi.org/10.1021/nl104227t.

[24] T. Kondo *et al.*, “Investigation of electrical contacts on a nanometer scale using a Nano-manipulator in Scanning Electron Microscope,” *2015 IEEE 61st Holm Conference on Electrical Contacts (Holm)*, pp. 262–265, 2015, doi: 10.1109/HOLM.2015.7355107.

[25] I. N. Sneddon, “Boussinesq’s problem for a rigid cone,” *Mathematical Proceedings of the Cambridge Philosophical Society*, vol. 44, no. 4, pp. 492–507, 1948, doi: 10.1017/S0305004100024518.

[26] C. Saringer, M. Tkadletz, M. Kratzer, and M. J. Cordill, “Direct determination of the area function for nanoindentation experiments,” *J Mater Res*, vol. 36, no. 11, pp. 2154–2165, Jun. 2021, doi: 10.1557/s43578-021-00113-9.

[27] M. Galetto, J. Kholkhujaev, and G. Maculotti, “Improvement of instrumented indentation test accuracy by data augmentation with electrical contact resistance,” *CIRP Annals*, vol. 72, no. 1, pp. 469–472, Jan. 2023, doi: 10.1016/j.cirp.2023.03.034.

[28] A. Bolshakov and G. M. Pharr, “Influences of pileup on the measurement of mechanical properties by load and depth sensing indentation techniques,” vol. 13, no. 4, pp. 1049–1058, 1998.

[29] S. P. Baker and J. Liu, “Nanoindentation Techniques,” *Reference Module in Materials Science and Materials Engineering*, no. July 2015, pp. 1–9, 2016, doi: 10.1016/b978-0-12-803581-8.02586-8.

[30] W. C. Oliver and G. M. Pharr, “An improved technique for determining hardness and elastic modulus using load and displacement sensing indentation experiments,” *J Mater Res*, vol. 7, pp. 1564–1583, 1992, doi: https://doi.org/10.1557/JMR.1992.1564.

[31] L. Fang, C. L. Muhlstein, J. G. Collins, A. L. Romasco, and L. H. Friedman, “Continuous electrical in situ contact area measurement during instrumented indentation,” *J Mater Res*, vol. 23, no. 9, pp. 2480–2485, Sep. 2008, doi: 10.1557/JMR.2008.0298.

[32] S. Ruffell, J. E. Bradby, J. S. Williams, and O. L. Warren, “An in situ electrical measurement technique via a conducting diamond tip for nanoindentation in silicon,” *J Mater Res*, vol. 22, no. 3, pp. 578–586, 2007, doi: 10.1557/JMR.2007.0100.

[33] G. Singh, R. L. Narayan, A. M. Asiri, and U. Ramamurty, “Discrete drops in the electrical contact resistance during nanoindentation of a bulk metallic glass,” *Appl Phys Lett*, vol. 108, no. 18, p. 181903, 2016, doi: 10.1063/1.4948540.

[34] S. Comby-Dassonneville, F. Volpi, G. Parry, D. Pellerin, and M. Verdier, “Resistive-nanoindentation: contact area monitoring by real- time electrical contact resistance measurement,” *MRS Commun*, 2019, doi: 10.1557/mrc.2019.74.

[35] F. Volpi *et al.*, “Resistive-nanoindentation on gold: Experiments and modeling of the electrical contact resistance,” *Review of Scientific Instruments*, vol. 92, no. 3, 2021, doi: 10.1063/5.0032682.

[36] F. Volpi *et al.*, “Development of a multifunctional nanoindenter integrated in-situ Scanning Electron Microscope - application to the monitoring of piezoresponse and electro-mechanical failures,” *Thin Solid Films*, vol. 735, no. August, p. 138891, 2021, doi: 10.1016/j.tsf.2021.138891.

[37] M. Rusinowicz *et al.*, “Failure of a brittle layer on a ductile substrate: Nanoindentation experiments and FEM simulations,” *J Mech Phys Solids*, vol. 163, no. March, p. 104859, 2022, doi: 10.1016/j.jmps.2022.104859.

[38] B. A. Y. Volkov, “Improvements to the Microstructure and Physical Properties of Pd-Cu-Ag Alloys,” *Platinum Metals Rev.*, vol. 48, no. 1, pp. 3–12, 2004.

[39] S. P. Dimitrijević, B. D. Vurdelja, S. B. Dimitrijević, F. M. Veljković, Å. J. Kamberović, and S. R. Veličković, “Complementary methods for characterization of the corrosion products on the surface of Ag60Cu26Zn14 and Ag58.5Cu31.5Pd10 brazing alloys,” *Corrosion Reviews*, vol. 38, no. 2, pp. 111–125, 2020, doi: 10.1515/corrrev-2019-0067.

[40] M. M. McDonald, D. L. Keller, C. R. Heiple, and W. E. Hofmann, “Wettability of brazing filler metals on molybdenum and tzm,” *Weld J*, no. October, pp. 389–395, 1989.

[41] F. Houzé, R. Meyer, O. Schneegans, and L. Boyer, “Imaging the local electrical properties of metal surfaces by atomic force microscopy with conducting probes,” *Appl Phys Lett*, vol. 69, no. 13, p. 1975, Aug. 1996, doi: 10.1063/1.117179.

[42] J. il Jang and G. M. Pharr, “Influence of indenter angle on cracking in Si and Ge during nanoindentation,” *Acta Mater*, vol. 56, no. 16, pp. 4458–4469, Oct. 2008, doi: 10.1016/j.actamat.2008.05.005.

[43] P. G. Slade, *Electrical Contacts: Principles and Applications, Second Edition*. CRC Press, 2014. Accessed: Dec. 12, 2021. [Online]. Available: https://books.google.fr/books?hl=fr&lr=&id=_ghEDwAAQBAJ&oi=fnd&pg=PP1&dq=P.+G.+Slade,+Electrical+Contacts+:+Principles+and+Applications,+2nd+ed.+CRC+Press,+2014&ots=do3bmtWgXf&sig=0Zb1GzgVMoosm_dN62Qb3i1eeMc#v=onepage&q&f=false

[44] K. Durst, M. Göken, and H. Vehoff, “Finite element study for nanoindentation measurements on two-phase materials,” *J Mater Res*, vol. 19, no. 1, pp. 85–93, 2003, doi: 10.1557/jmr.2004.0010.

[45] W. D. Nix and H. Gao, “Indentation size effects in crystalline materials: A law for strain gradient plasticity,” *J Mech Phys Solids*, vol. 46, no. 3, pp. 411–425, 1998, doi: 10.1016/S0022-5096(97)00086-0.